



Porous N–C catalyst synthesized by pyrolyzing g-C₃N₄ embedded in carbon as highly efficient oxygen reduction electrocatalysts for primary Zn-air battery

Li Zhang ^{a,1}, Jing Xiong ^{b,1}, Yuan-Hang Qin ^{a,*}, Cun-Wen Wang ^{b,**}

^a Key Laboratory of Green Chemical Process of Ministry of Education, School of Chemical Engineering and Pharmacy, Wuhan Institute of Technology, Wuhan, 430205, China

^b Key Laboratory of Novel Reactor and Green Chemical Technology of Hubei Province, School of Chemical Engineering and Pharmacy, Wuhan Institute of Technology, Wuhan, 430205, China

ARTICLE INFO

Article history:

Received 18 March 2019

Received in revised form

17 May 2019

Accepted 18 May 2019

Available online 21 May 2019

ABSTRACT

Nitrogen-doped carbon (N–C) materials are promising low-cost catalysts for oxygen reduction reaction (ORR). However, the commonly used route for N–C synthesis, viz., the high-temperature pyrolysis of N- and C-containing precursors, usually results in a great loss of N-containing species determining the ORR catalytic performance. Herein, porous N–C materials are synthesized by using g-C₃N₄ embedded in glucose-derived carbon as template and N source. The N–C sample synthesized at 900 °C with a mass ratio of glucose to g-C₃N₄ being 4:1 exhibits a positive half-wave potential ($E_{1/2} = 0.823$ V), good long-term stability and dominant 4 e[−] pathway for ORR in alkaline media, which can be attributed to its large specific surface area, high porosity, and large fraction of pyridinic and graphitic N. When a small amount of Fe is doped into the N–C sample, its ORR performance can be greatly improved and outperforms the commercial Pt/C catalyst in terms of ORR activity ($E_{1/2} = 0.880$ V), long-term stability and methanol tolerance. Notably, primary Zn-air batteries with N–C and Fe–N–C being the cathode catalysts exhibit peak power densities of 88 and 100 mW cm^{−2}, respectively. This work offers a promising route for the synthesis of porous carbon-based materials highly efficient as ORR catalyst for Zn-air battery.

© 2019 Elsevier Ltd. All rights reserved.

1. Introduction

In the past decade, electrochemical energy storage and conversion (EESC) devices have attracted great attention because of the growing demand for renewable energy as well as the increasing concern about environmental problems resulting from the fossil energy use [1]. Among EESC devices, metal-air batteries are gaining attention because of their high specific energy density [2]. In particular, Zn-air battery is gaining particular attention because of its low cost, high abundance, environmental benignity, etc [3]. Oxygen reduction reaction (ORR) is a key reaction in Zn-air battery [4]. At present, the most commonly used ORR catalysts are Pt-based materials. However, the high cost, limited reservoir and poor long-

term stability of Pt greatly limit its practical use. Therefore, developing non-precious ORR catalysts for Zn-air battery has attracted great attention in recent years. Among the various non-precious ORR catalysts developed, nitrogen-doped carbon (N–C) materials have been generally considered to be the promising ones [4,5]. Although the origin of ORR activity of N–C materials is still controversial [6,7], it is broadly recognized that the nitrogen species especially pyridinic N plays an important role in catalyzing ORR [8]. The synthesis of N–C materials for ORR generally involves the high-temperature pyrolysis of C- and N-containing precursors, and the as-synthesized N–C materials often contain complicated N species at low concentration, largely due to the limited N content in the precursor and the high loss of N species at high temperature [9]. Therefore, selecting an appropriate N-containing precursor with high N content and at the same time alleviating N loss during pyrolysis are highly desirable.

Graphitic carbon nitride (g-C₃N₄) is a sheet-like framework containing 57 at. % nitrogen and 43 at. % carbon. Although containing large quantities of pyridinic-like N, g-C₃N₄ itself is not an

* Corresponding author.

** Corresponding author.

E-mail addresses: qyhsir@qq.com, yhqin@wit.edu.cn (Y.-H. Qin), wangcw0120@163.com (C.-W. Wang).

¹ These authors contribute equally to this work.

efficient ORR catalyst due to its low electron transfer ability resulting from its semiconductive property. To address this issue, the most frequently used method is to support the semiconductive $g\text{-C}_3\text{N}_4$ on a conductive substrate. Qiao et al. supported $g\text{-C}_3\text{N}_4$ on CMK-3 mesoporous carbon and found that the obtained $g\text{-C}_3\text{N}_4\text{@CMK-3}$ composite exhibited competitive catalytic activity to commercial Pt/C catalyst for ORR in alkaline media [10]. Recently, Qiao et al. supported $g\text{-C}_3\text{N}_4$ coordinated transition metals (M) on CNT and found that the obtained M- $g\text{-C}_3\text{N}_4\text{/C}$ catalysts possessed comparable activity to that of the commercial Pt/C catalyst for ORR in alkaline media [9]. However, the $g\text{-C}_3\text{N}_4$ -based catalysts, neither $g\text{-C}_3\text{N}_4\text{@CMK-3}$ nor M- $g\text{-C}_3\text{N}_4\text{/C}$ demonstrated ORR performance in alkaline media comparable to their state-of-the-art counterparts, indicating that $g\text{-C}_3\text{N}_4$ -supported on conductive carbon substrate still cannot fully exploit the benefits of $g\text{-C}_3\text{N}_4$ as precursor for ORR catalyst.

Considering that $g\text{-C}_3\text{N}_4$ only contains N and C elements, directly converting it to N–C materials by high-temperature pyrolysis is of interest. However, when $g\text{-C}_3\text{N}_4$ alone was pyrolyzed at temperature higher than 700 °C, the temperature at which N–C materials was usually formed, no solid product was obtained even under inert atmosphere, because the complete decomposition of $g\text{-C}_3\text{N}_4$ into C- and N-containing gases occurred at high temperature [11]. Inspired by this fact, in this work, $g\text{-C}_3\text{N}_4$ embedded in conductive carbon substrate rather than supported on conductive carbon substrate was explored to synthesize the $g\text{-C}_3\text{N}_4$ -based ORR catalyst by high-temperature pyrolysis. In this way, porous N–C materials were synthesized by using the N source and removable template provided by $g\text{-C}_3\text{N}_4$ embedded in conductive carbon substrate during the pyrolysis process. In addition, the synthesis of $g\text{-C}_3\text{N}_4$ -based Fe–N–C materials as ORR catalyst was also carried out and their use as air catalyst for primary Zn-air battery was explored.

2. Experimental

2.1. Synthesis of N–C and Fe–N–C catalysts

$g\text{-C}_3\text{N}_4$ was synthesized by pyrolyzing urea (AR, Xilong Scientific Co., Ltd.) loaded in a covered corundum crucible at 550 °C for 4 h with a heating rate of 5 °C min^{−1}. The N–C catalyst was synthesized by a two-step process: hydrothermal carbonization and high-temperature pyrolysis. A suspension containing 40 mL of H₂O (18.2 MΩ cm), 0.5 g of $g\text{-C}_3\text{N}_4$, and desired amount of glucose (GR, Shanghai Macklin Biochemical Co., Ltd.) was ultrasonicated for 4 h (350 W, 40 kHz), and then the resulting suspension was transferred to a Teflon-lined autoclave (50 mL) and heated at 160 °C for 10 h. The resulting sample was centrifuged and washed three times alternately with deionized water and ethanol. The resulting sample was dried at 80 °C overnight, grinded, and loaded into a covered corundum boat and then transferred to a tube furnace and pyrolyzed in N₂ atmosphere at desired temperature for 1 h with a heating rate of 5 °C min^{−1}. To synthesize the Fe–N–C catalyst, a suspension similar to that used for N–C synthesis but containing 30 mg of FeCl₃·6H₂O (AR, Shanghai Macklin Biochemical Co., Ltd.) was used in the hydrothermal carbonization step, and the other parameters and procedures were the same as those used in the N–C catalyst synthesis.

2.2. Physical and electrochemical characterization

The structure and morphology of the as-synthesized materials were characterized by X-ray diffraction (XRD, D8 Advance, Bruker), transmission electron microscopy (TEM, JEM-2100, JEOL), high-resolution TEM (HRTEM, FEI Titan Themis 200) equipped with an

energy dispersive X-ray spectrometer (EDX, Bruker Super-X), and X-ray photoelectron spectroscopy (XPS, VG Multilab 2000). The specific surface area and pore size distribution of the as-synthesized materials were determined by a surface area and porosity analyzer (ASAP2460, Micromeritics). The electrochemical characterization was performed on an electrochemical workstation (PGSTAT 302 N, Metrohm Autolab) in a three-electrode cell consisting of a graphite rod counter electrode, a calibrated Hg/HgO reference electrode, and a catalyst sample-modified glassy carbon (GC, 3 mm in diameter) working electrode. All the potentials in this work were reported with respect to the reversible hydrogen electrode (RHE). For preparation of the working electrode, the catalyst ink was firstly prepared by sonicating 6 mg of catalyst sample in a mixture of water (800 μL), ethanol (200 μL) and Nafion (5 wt %) solution (80 μL), then 5 μL of the catalyst ink was carefully cast onto the GC electrode, and after solvent evaporation the finally obtained electrode was served as the working electrode. For comparison, the GC electrode cast with 132 μg cm^{−2} of Pt/C catalyst (20 wt %, Johnson Matthey) was also prepared. KOH solution (0.1 M) maintained at 25 °C with circulating ethylene glycol/water was used as the electrolyte. Before ORR performance test, the working electrode was first subject to fifty continuous cyclic voltammetry (CV) scans between 0 and 1 V vs. RHE at 50 mV s^{−1} in N₂-saturated 0.1 M KOH solution. The ORR performance of catalyst was measured in O₂-saturated 0.1 M KOH solution by using the rotating-disk electrode (RDE) technique with linear sweep voltammetry (LSV) at 10 mV s^{−1}. The number (*n*) of electrons transferred in the ORR process was determined based on the Koutecky-Levich (K-L) Equation [12]. The rotating ring-disk electrode (RRDE, Pine) technique was used to determine the HO₂[−] yield and the electron transfer number *n* according to the following equations [13],

$$\text{HO}_2^-(\%) = 200 \frac{I_r/N}{I_d + I_r/N} \quad (1)$$

$$n = 4 \frac{I_d}{I_d + I_r/N} \quad (2)$$

where *I_r* and *I_d* are the ring current and disk current, respectively, and *N* is the collecting efficiency of Pt ring (0.37).

A primary Zn-air battery with carbon paper-supported N–C or Fe–N–C (catalyst loading of ca. 1 mg cm^{−2}) as cathode and a Zn foil (thickness of 0.5 mm) as anode was constructed. The battery performance was investigated by using 6 M KOH solution as electrolyte.

3. Results and discussion

Fig. 1(a) shows the procedure for N–C synthesis. Firstly, $g\text{-C}_3\text{N}_4$ was synthesized by pyrolyzing urea and then the urea-derived $g\text{-C}_3\text{N}_4$ was used as N source and template for N–C synthesis, which was realized by a two-step process consisting of a hydrothermal (HT) carbonization process and a high-temperature pyrolysis process. In the hydrothermal carbonization process, glucose under hydrothermal conditions first underwent a polymerization process in which some linear or branchlike oligosaccharides were formed and then these obtained oligosaccharides underwent a carbonization step arising from the cross-linking induced by intermolecular dehydration [14]. When $g\text{-C}_3\text{N}_4$ was present, glucose under the hydrothermal conditions could form carbon particles deposited on $g\text{-C}_3\text{N}_4$ (denoted as $g\text{-C}_3\text{N}_4\text{@C}$), due to the template role of $g\text{-C}_3\text{N}_4$. In the pyrolysis process, $g\text{-C}_3\text{N}_4\text{@C}$ was converted to porous N–C materials with the embedded $g\text{-C}_3\text{N}_4$ serving as N source and removable template.

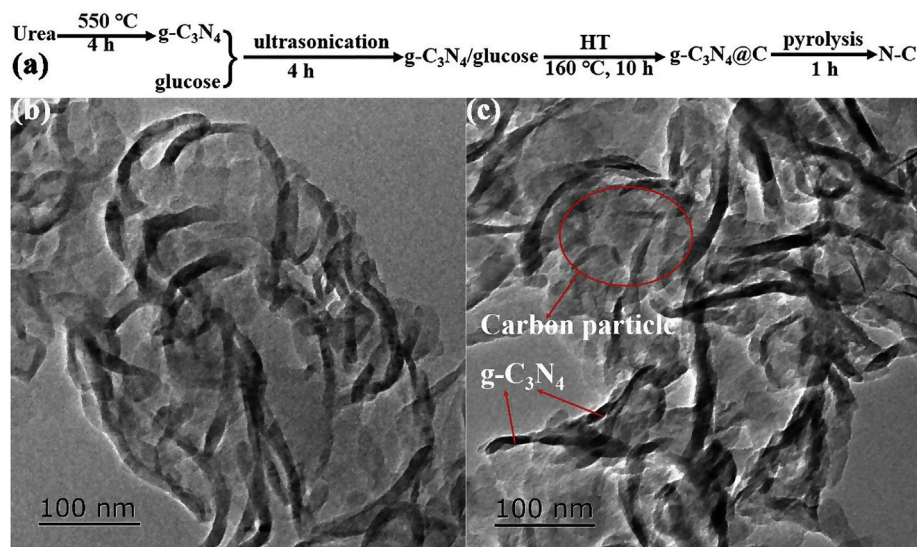


Fig. 1. The procedure for N–C synthesis (a), and the TEM images of g-C₃N₄ (b) and g-C₃N₄@C (c). (A colour version of this figure can be viewed online.)

Fig. 1(b) shows the TEM image of the as-synthesized g-C₃N₄, where one can find that the obtained g-C₃N₄ sheets demonstrate a wrinkled morphology, which is the characteristic morphology of urea-derived g-C₃N₄ [15]. Fig. 1(c) shows the morphology of g-C₃N₄@C synthesized with the mass ratio of g-C₃N₄ to glucose being 1:4. It can be observed that carbon particles are uniformly deposited on the g-C₃N₄ surface, and the carbon particles serve to provide C source while the embedded g-C₃N₄ sheets serve to provide N source for N–C synthesis.

Since the mass ratio of C source (glucose) to N source (g-C₃N₄) may influence the morphology and N doping level of the synthesized N–C materials, g-C₃N₄ to glucose of the mass ratios of 1:2, 1:4 and 1:6 were investigated and the obtained samples were denoted as N–C-2, N–C-4 and N–C-6, respectively. Fig. 2 shows the TEM images of N–C materials synthesized at 900 °C with different mass ratios of g-C₃N₄ to glucose. It can be seen that all the three N–C samples present a wrinkled nanosheet-like morphology, which is similar to the inverted replica of g-C₃N₄, although with much thinner nanosheets, confirming the sacrificing template role of g-C₃N₄. Notably, the N–C nanosheets become thicker with increasing mass ratio of glucose to g-C₃N₄, which can be attributed to the fact that more glucose can deposit a thicker carbon coating on g-C₃N₄ in the hydrothermal process, which thus can produce a thicker nanosheet in the pyrolysis process.

The morphology of N–C-4 was further characterized by HRTEM. The high-angle annular dark-field scanning TEM (HAADF-STEM) image (Fig. 3(a)–(b)) shows that the N–C-4 sample consists of

several conductive graphitic layers of wrinkled nanosheets full of pores, such a porous structure can provide exposed active sites for ORR and ensure rapid pathways for mass transfer during ORR process, thus enhancing the ORR performance of N–C sample. The HAADF-STEM image and the corresponding elemental mapping images (Fig. 3(c)–(f)) confirm that the N elements are densely and uniformly dispersed on the entire nanosheets along with C elements. Because it is broadly accepted that the active sites for ORR in N–C catalysts are related with N species [8], the dense and uniform dispersion of N elements implies that the potential active sites are densely and uniformly dispersed throughout the N–C sample.

The N₂ adsorption-desorption isotherms of N–C samples (Fig. 4(a)), which can be assigned to the type IV isotherm with type H3 distinct hysteric loops [16], combined with the Barrett-Joyner-Halenda (BJH) pore size distribution curves of N–C samples (Fig. 4(b)), together indicating the mesopore-dominant porous structure of the as-synthesized N–C samples. It can be seen that both Brunauer-Emmett-Teller (BET) surface area and pore volume of the as-synthesized N–C samples decrease with increasing mass ratio of glucose to g-C₃N₄, which is consistent with the above TEM characterization results that the nanosheets of N–C samples become thinner with decreasing mass ratio of glucose to g-C₃N₄. Notably, the as-synthesized N–C samples have a pore volume larger than 1 cm³ g^{−1}, further verifying the removable template role of g-C₃N₄. Such a large pore volume can enable the as-synthesized N–C sample to host a large number of easily accessible active sites and provide facilitated pathways for the transportation of ORR-

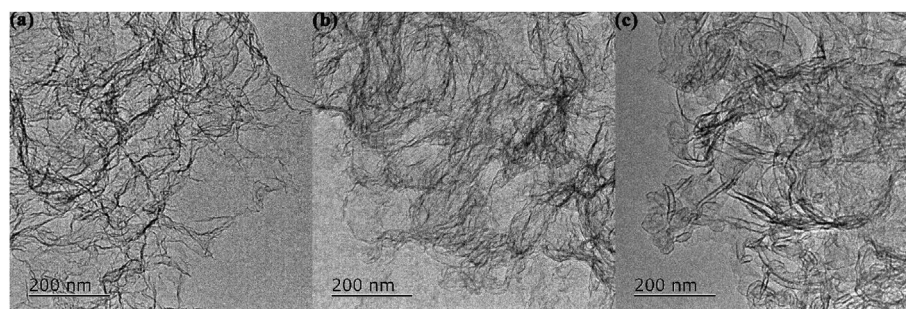


Fig. 2. TEM images of N–C-2 (a), N–C-4 (b) and N–C-6 (c).

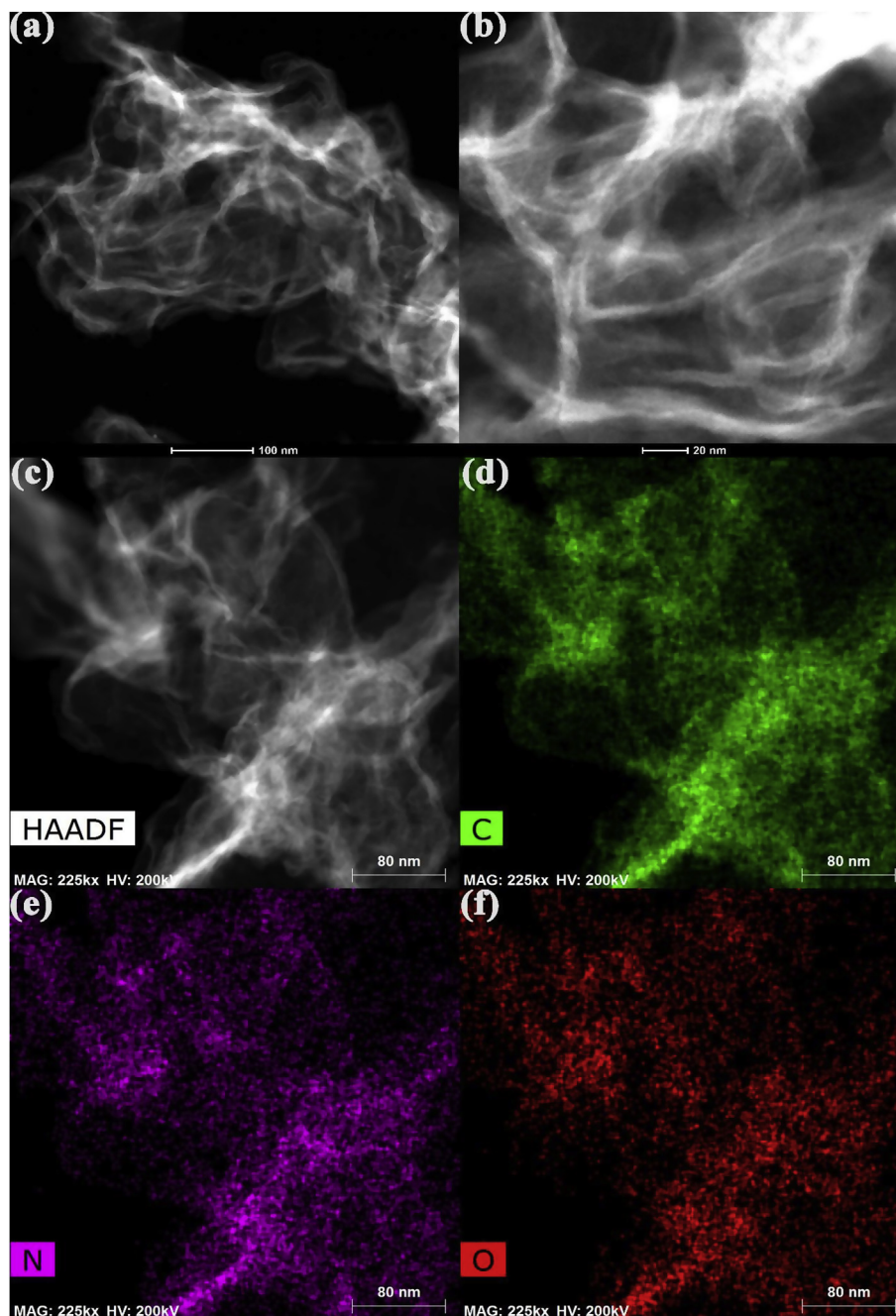


Fig. 3. HAADF-STEM images of N–C-4 (a–b), and HAADF-STEM image (c) and the corresponding elemental mapping images of C (d), N (e) and O (f). (A colour version of this figure can be viewed online.)

involved species [17], thus promoting its ORR performance.

The structural characteristics of N–C samples was further characterized by XRD and the results are shown in Fig. 4(c). It can be seen that all the three N–C samples present a broad diffraction peak centered at ca. 24° , which can be attributed to the (002) plane of carbon [18]. The graphitization degree of N–C samples was evaluated by Raman technique. Fig. 4(d) shows the Raman spectra of the three N–C samples, in which all the three samples exhibit two obvious peaks at ca. 1580 and 1350 cm^{-1} , which are known to correspond to the graphite crystallite component and the graphite disorder in carbon materials, respectively [19,20]. The relative intensity ratio I_{1350}/I_{1580} can be used to estimate the graphitization degree of carbon-based materials [21]. The smaller the intensity

ratio, the higher the graphitization degree. The intensity ratio of I_{1350}/I_{1580} was calculated to be ca. 1.10 for each N–C sample. No obvious difference in I_{1350}/I_{1580} indicates that the mass ratio of glucose to g- C_3N_4 has no obvious effect on the graphitization degree of the resulting N–C samples.

The chemical composition of N–C samples was further investigated by XPS, as shown in Fig. S1, which confirms the successful doping of N into the carbon matrix. N doping can increase the electrophilicity of the resulting carbon materials and create active sites for ORR [22]. Notably, all the N–C samples have a N content larger than 10 at. %, indicating of the successful role played by g- C_3N_4 as N source. Interestingly, N–C-4 presents the lowest N doping level among the three N–C samples (Table S1), which is not

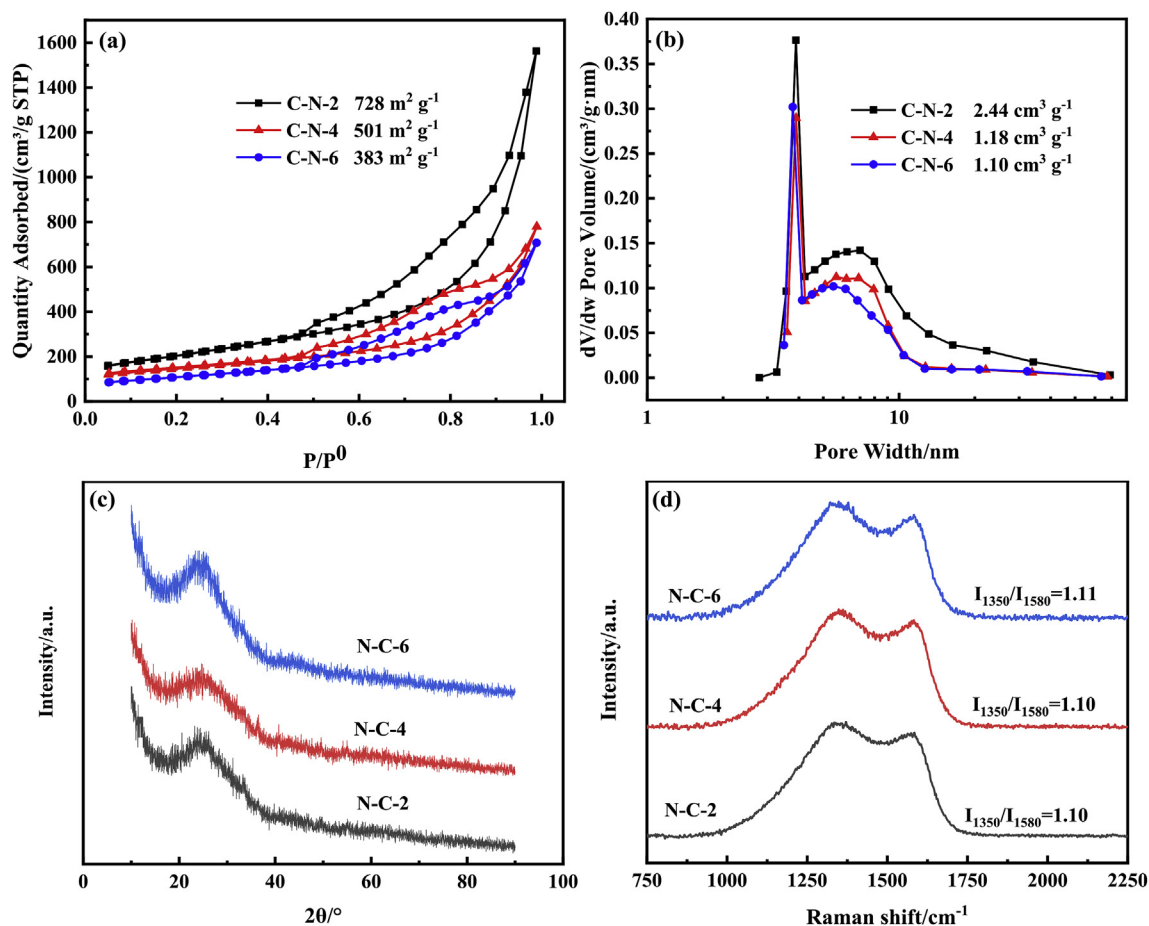


Fig. 4. N₂ adsorption-desorption isotherms (a), pore size distribution curves (b), XRD (c) and Raman (d) patterns of N-C samples. (A colour version of this figure can be viewed online.)

consistent with the expectation that the N doping level will decrease with increasing mass ratio of glucose to g-C₃N₄. The lowest N doping level presented by N-C-4 may result from the following reasons. In the hydrothermal carbonization step, the carbon coating on g-C₃N₄ of N-C-4 is thinner than that of N-C-6, and correspondingly in the pyrolysis step N-C-4 has a higher loss of N-containing species due to the relatively poor covering of g-C₃N₄ by carbon coating, which makes N-C-4 presenting a lower N content than N-C-6. The C1s spectra of the N-C samples can be deconvoluted into five peaks with binding energies of ca. 284.6, 285.7, 286.4, 288.0 and 290.2 eV (Fig. S2), corresponding to C-C, C=C, C=N, C-N and C=O, respectively [23,24]. The N1s spectra of the N-C samples can be deconvoluted into four peaks with binding energies of ca. 398.0, 399.2, 400.1 and 403.2 eV (Fig. 5(a)-(c)), which can be assigned to pyridinic N, pyrrolic N, graphitic N and oxidized N, respectively [25–27]. Fig. 5(d) shows the relative content of the four N-containing species in N-C samples. It can be seen that N-C-4 has the largest portions of pyridinic N and graphitic N. It is generally believed that the pyridinic N can modify the local electronic structure of carbon matrix and involve in the formation of active sites while the graphitic N can facilitate the 4 e⁻ pathway during the ORR process [22,28]. Therefore, N-C-4 with the largest portions of pyridinic N and graphitic N is expected to have a good ORR performance.

Fig. 6(a) shows the LSV curves of N-C and Pt/C catalysts. Interestingly, among the three N-C samples, N-C-4 exhibits the highest half-wave potential $E_{1/2}$ of 0.823 V vs. RHE, which is 30 mV more

negative than that of the Pt/C catalyst and comparable to or even better than those of the best N-C catalysts reported for ORR [26,29–31]. Considering the architectural and compositional properties of the three N-C samples, the relatively good ORR catalytic activity exhibited by N-C-4 may largely result from its relatively large fraction of pyridinic and graphitic N. Ruoff et al. found that the graphitic N in N-C sample could increase the limiting current density while the pyridinic N could decrease the overpotential for ORR [32]. Wang et al. and Xie et al. found that the N-C samples with relatively large fraction of graphitic and pyridinic N exhibited the best ORR activity [33,34]. As hydrolysis temperature is a very important parameter determining the ORR performance of N-C catalysts, the hydrolysis temperature for N-C-4 synthesis was optimized. As shown in Fig. S3, N-C-4 synthesized at 900 °C exhibited the most positive $E_{1/2}$, which might be because the N-C-4 sample synthesized at 800 °C has a lower electrical conductivity resulting from its lower graphitization degree (Fig. S4), while the N-C-4 sample synthesized at 1000 °C has a lower N content resulting from the higher loss of N-containing species at high temperature. Therefore, the pyrolysis temperature of 900 °C was selected to synthesize the N-C-4 sample.

The high ORR activity of N-C-4 is further evidenced by its Tafel slope of 62 mV dec⁻¹, which is even smaller than that of Pt/C catalyst (69 mV dec⁻¹), as shown in Fig. 6(b). The high ORR performance of N-C-4 can be rationally attributed to its favorable architectural and compositional features: (1) the porous N-C nanosheets with high specific surface area and large pore volume

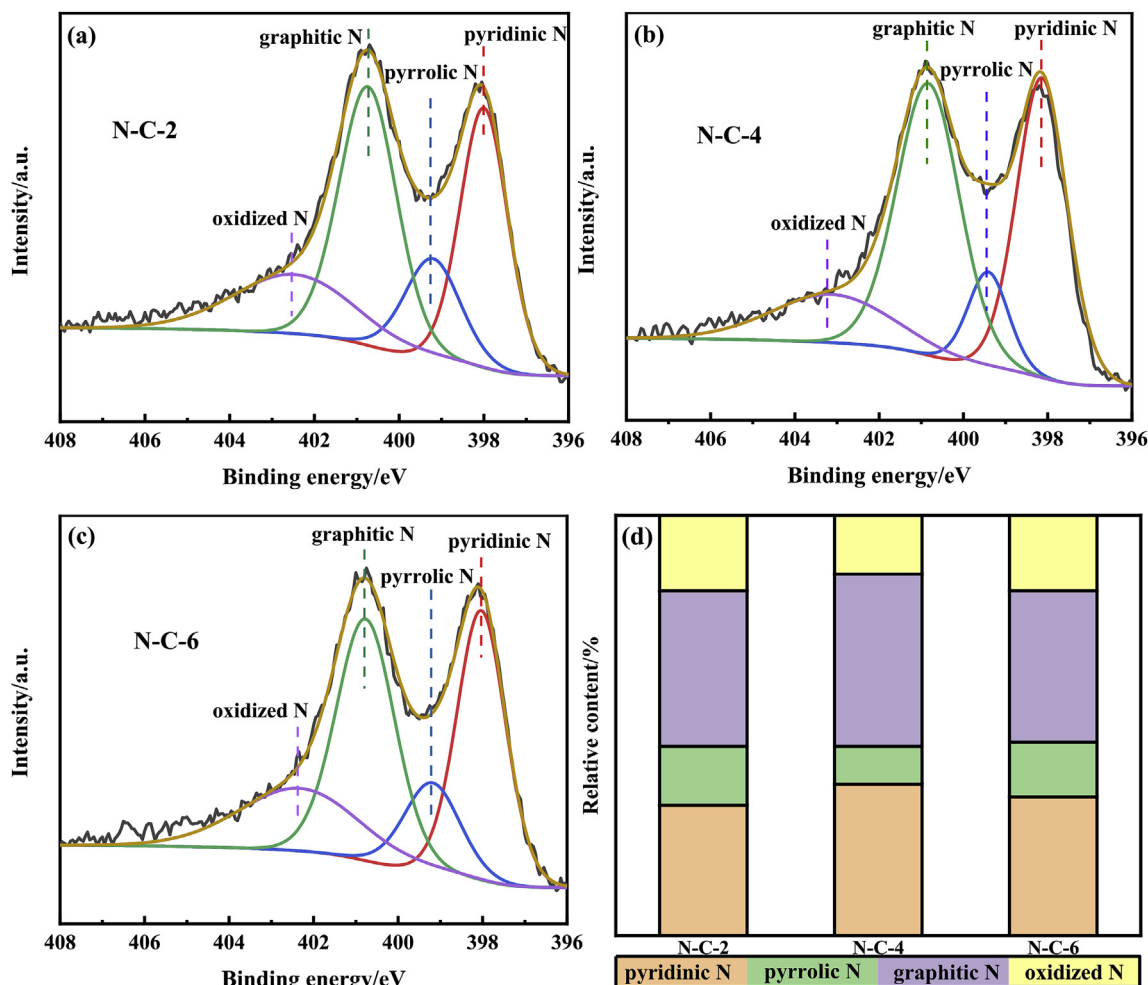


Fig. 5. High-resolution N1s XPS spectra (a–c) and the relative contents of the deconvoluted peak areas of N1s XPS spectra (d) for N–C samples. (A colour version of this figure can be viewed online.)

are able to afford a large number of fully accessible active sites for ORR and provide facilitated pathway for the mass transportation of ORR-involved species; (2) the high-fraction pyridinic and graphitic N in carbon matrix are conducive to the formation of active sites and the occurrence of $4 e^-$ pathway during the ORR process. LSV measurements using RDE technique were carried out to evaluate the ORR performance of N–C–4 sample (Fig. 6(c)). From the K–L plots (Fig. 6(c) inset) the ORR electron transfer numbers were determined based on the K–L equation, which are close to 4, indicating that ORR on N–C–4 sample may proceed in a dominant $4 e^-$ pathway.

To further determine the ORR pathway on N–C–4, RRDE measurement was performed and the corresponding electron transfer number determined was 3.51–3.96 in the potential range of 0.9–0 V (Fig. 6(d)), confirming the dominant $4 e^-$ pathway for ORR on N–C–4. To examine the methanol crossover effect on N–C–4, chronoamperometric response at 0.625 V vs. RHE was recorded. As shown in Fig. 6(e), there is a dramatic decrease in the current density on Pt/C after injecting 5 mL of methanol into 200 mL of 0.1 M KOH solution. In contrast, there is no obvious change in the current density on N–C–4, indicating that N–C–4 is highly methanol tolerant. The ORR stability of catalysts was evaluated by an accelerated durability test (ADT) protocol, which was carried out by cycling the catalyst-modified working electrode in the potential range of 0.6–1.0 V vs. RHE for 10000 cycles in O_2 -saturated 0.1 M

KOH solution with a scanning rate of 100 mV s^{-1} . After ADT the $E_{1/2}$ values are negatively shifted by 15 and 30 mV for N–C–4 and Pt/C, respectively (Fig. 6(f)), indicating that N–C–4 has a better long-term stability than Pt/C.

It is widely reported that doping Fe into N–C can greatly improve its ORR performance [25,35,36]. In this work, 30 mg of $\text{FeCl}_3 \cdot 6\text{H}_2\text{O}$ was added into the precursor for N–C–4 synthesis and the obtained sample was denoted as Fe–N–C–4. Fig. 7(a) shows the TEM image of Fe–N–C–4 sample, which presents a similar image as that of N–C–4, indicating that the Fe doping did not change the morphology of N–C sample. Notably, no Fe-based particles can be observed, indicating that the formation of large Fe-based particles were greatly suppressed, which is desirable because recently single Fe atom/cluster dispersed on N–C as ORR catalyst has received great attention because of its good ORR performance [17,36]. Fig. 7(b)–(f) show the HAADF-STEM and corresponding elemental mapping images of Fe–N–C–4. It can be seen that the Fe elements are finely and highly dispersed on the N–C matrix, although the single Fe atom/cluster cannot be observed from HAADF-STEM image of Fe–N–C–4 sample. The fine and uniform dispersion of Fe species on N–C matrix may largely result from the effect of g- C_3N_4 , which is reported to be able to anchor Fe ions for the conversion of Fe–N/C complex in the pyrolysis process [9,37,38].

Fig. 8(a) shows the LSV curve of Fe–N–C–4. It can be seen that the Fe–N–C–4 catalyst exhibits a $E_{1/2}$ of 0.880 V vs. RHE, which is

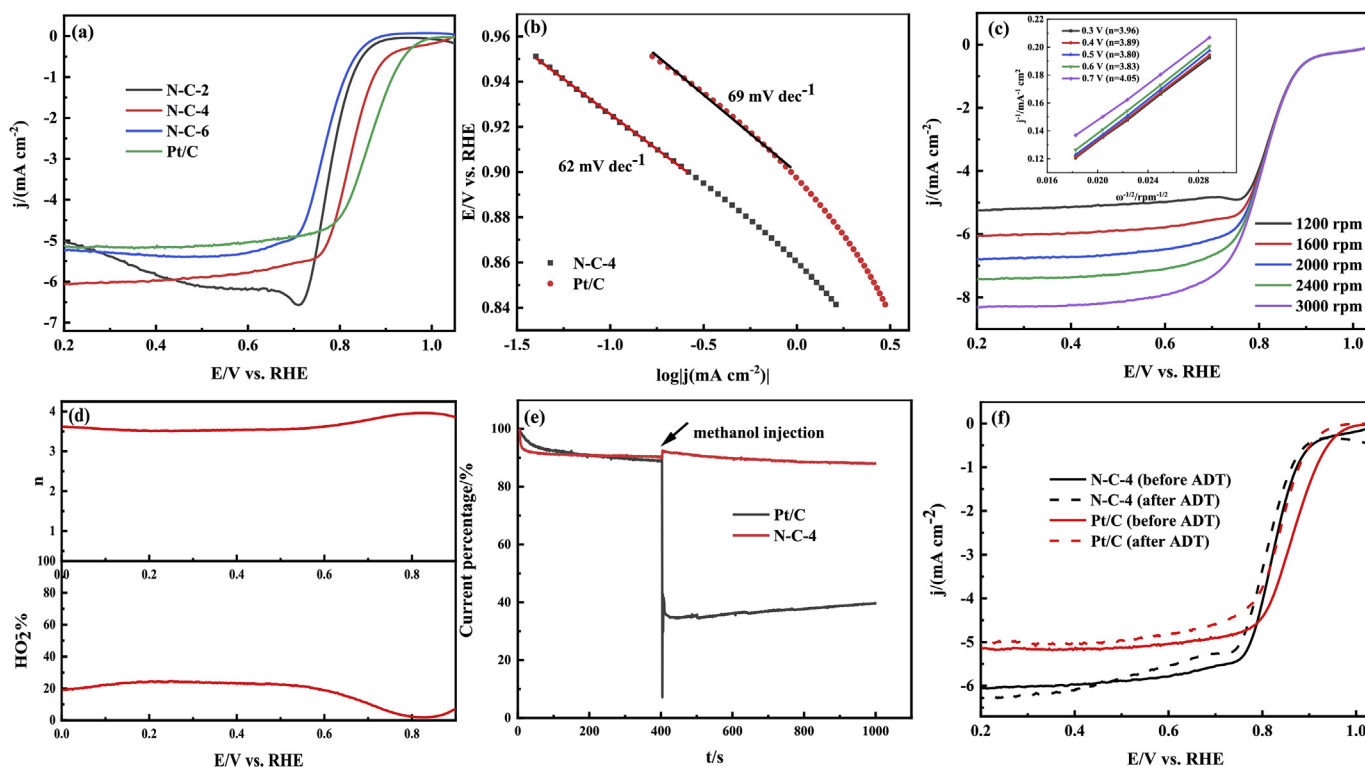


Fig. 6. LSV curves recorded in O₂-saturated 0.1 M KOH solution at 1600 rpm (a), Tafel plots (b), RDE curves and K-L plots of N-C-4 catalyst (c), plots of HO₂⁻ yield and electron transfer number of N-C-4 (d), chronoamperometric tests of N-C-4 and Pt/C catalysts (e), and LSV curves of N-C-4 and Pt/C catalysts before and after ADT (f). (A colour version of this figure can be viewed online.)

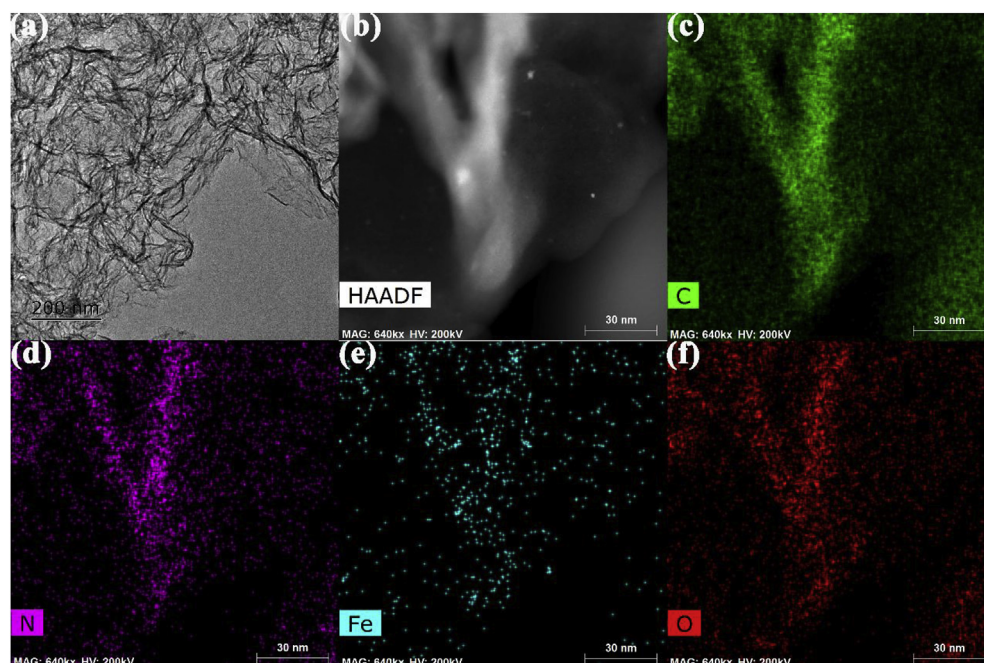


Fig. 7. TEM image (a), and HAADF-STEM image (b) and the corresponding elemental mapping images of C (c), N (d), Fe (e) and O (f) of Fe-N-C-4 sample. (A colour version of this figure can be viewed online.)

57 mV more positive than that of N-C-4 catalyst, 27 mV more positive than that of the Pt/C catalyst (0.853 V vs. RHE) and comparable to or even better than those of the best nonprecious catalysts recently reported (Table S2). The high ORR activity of Fe-N-C-

4 catalyst is further evidenced by its Tafel slope of 58 mV dec⁻¹, as shown in Fig. 8(b). LSV measurements were carried out to evaluate the ORR performance of Fe-N-C-4 sample by using the RDE technique (Fig. 10(c)). The ORR electron transfer numbers

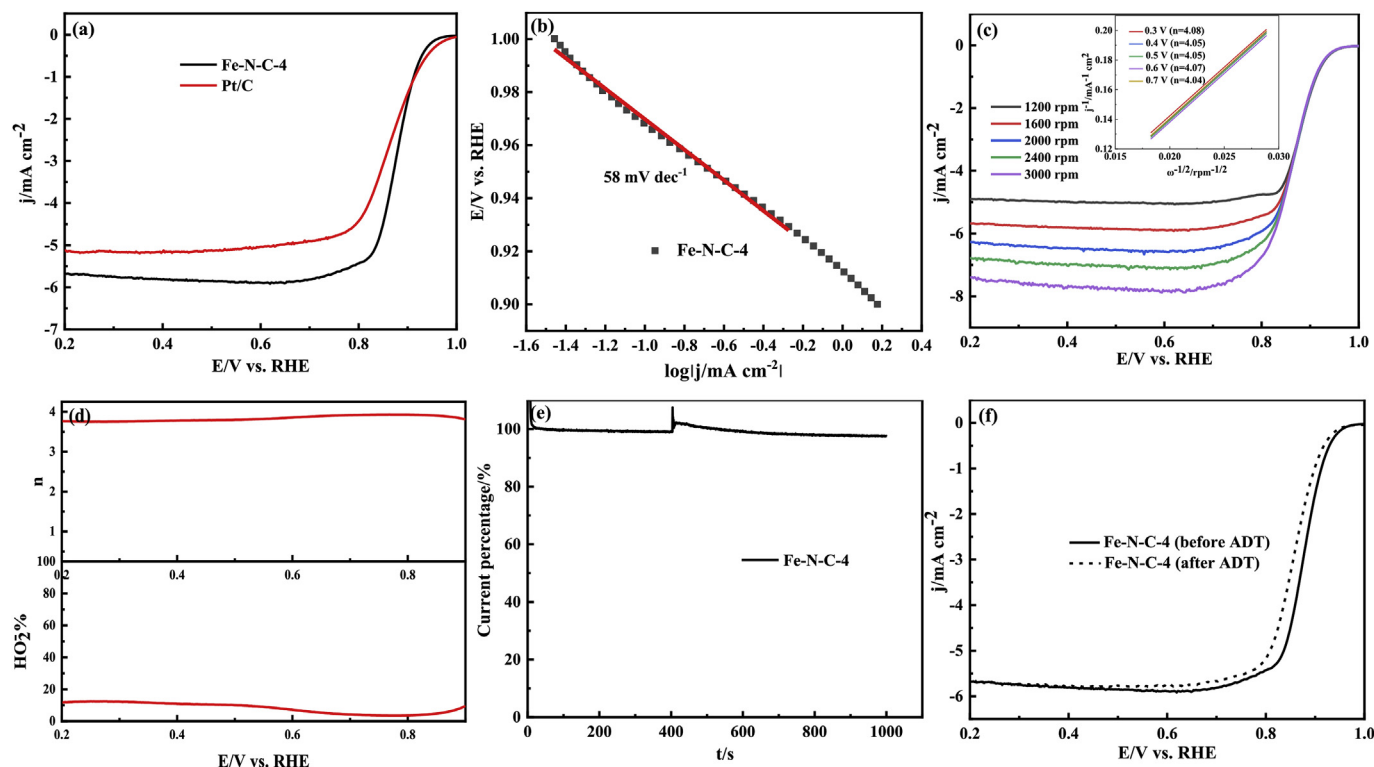


Fig. 8. LSV curves of Fe–N–C–4 recorded in O₂-saturated 0.1 M KOH solution at 1600 rpm (a), Tafel plots of Fe–N–C–4 (b), RDE curves and K–L plots of Fe–N–C–4 (c), plots of HO₂[−] yield and electron transfer number of Fe–N–C–4 (d), chronoamperometric tests of Fe–N–C–4 (e), and LSV curves of Fe–N–C–4 before and after ADT (f). (A colour version of this figure can be viewed online.)

determined based on the K–L equation are rather close to 4 (Fig. 8(c) inset), evidencing the dominant 4 e[−] pathway for Fe–N–C–4 catalyst.

To further determine the ORR pathway on Fe–N–C–4 catalyst, RRDE measurement was performed (Fig. 8(d)). The corresponding electron transfer number determined for Fe–N–C–4 catalyst is 3.75–3.93 in the potential range of 0.9–0.2 V vs. RHE, which is slightly larger than that for N–C–4 catalyst, evidencing the important role played by Fe during ORR. The high ORR activity of Fe–N–C–4 can be mainly attributed to the favorable architectural and compositional features of N–C as well as its own feature, that is, the highly dispersed Fe-based species is able to work cooperatively with the N–C nanosheets to boost the ORR performance. The methanol tolerance of Fe–N–C–4 catalyst was examined by the above chronoamperometric technique and the result (Fig. 8(e)) shows that there is no obvious change in the current density on Fe–N–C–4, indicating that Fe–N–C–4 is free from the methanol crossover effect. The ORR stability of Fe–N–C–4 catalyst was evaluated using the above ADT protocol, and the results show that after ADT the $E_{1/2}$ of Fe–N–C–4 is decreased by 19 mV (Fig. 8(f)), 11 mV more less than that of Pt/C catalyst. In addition, the diffusion-limiting current density of Fe–N–C–4 after ADT is slightly decreased, while that of Pt/C is significantly decreased (Fig. 6(f)), further indicating that Fe–N–C–4 has a better long-term stability than Pt/C catalyst.

Motivated by N–C–4 and Fe–N–C–4 (abbreviated as N–C and Fe–N–C) catalysts' superior ORR performance, their use as cathode catalyst for primary Zn–air battery was explored. It can be seen from Fig. 9(a) that N–C- and Fe–N–C-based Zn–air batteries exhibit open-circuit voltages of ca. 1.47 and 1.51 V, respectively. From Fig. 9(b) it can be seen that the peak power densities are 88 and 100 mW cm^{−2} for N–C- and Fe–N–C-based Zn–air batteries,

respectively, which are larger than those of the recently reported Zn–air batteries based on 200-CNTs–Co/NC (83.1 mW cm^{−2}) [39], NPMC-1000 (55 mW cm^{−2}) [40], N–GRW (65 mW cm^{−2}) [41]. The large power density of N–C- and Fe–N–C-based Zn–air batteries may largely result from the large pore volume in the catalyst layer which provides fully accessible active sites for ORR and ensure rapid pathway for the mass transportation of ORR-involved species [42]. At the discharge current density of 10 mA cm^{−2}, Fe–N–C delivers a discharge voltage plateau of ca. 1.25 V with negligible voltage decay over 6 h of discharge (Fig. 9(c)), and N–C exhibits a slight voltage decay, indicating that both materials as cathode catalyst for Zn–air batteries have good stability. Moreover, the Zn–air batteries with N–C or Fe–N–C as the cathode catalyst was used to power a blue-light light-emitting diode (LED, 3.0 V) lamp, and it can be seen from Fig. 9(d) that the blue-light LED lamp could be powered by two Zn–air batteries in series, again confirming that the as-synthesized porous N–C and Fe–N–C materials have great potential for application in Zn–air batteries.

4. Conclusions

N–C samples were synthesized by selecting g-C₃N₄ embedded in glucose-derived carbon as N source and removable template. The N–C sample synthesized with the mass ratio of glucose to g-C₃N₄ being 4:1 exhibits a dominant 4 e[−] pathway for ORR and good catalytic activity ($E_{1/2}$ of 0.823 V), long-term stability and methanol tolerance. The ORR performance of N–C sample can be much improved by adding a small amount of Fe into the precursor and the obtained Fe–N–C sample exhibits a remarkable ORR catalytic activity ($E_{1/2}$ of 0.880 V), good long-term stability and excellent methanol tolerance as compared with the commercial Pt/C catalyst. The good ORR performance of the as-synthesized N–C and Fe–N–C

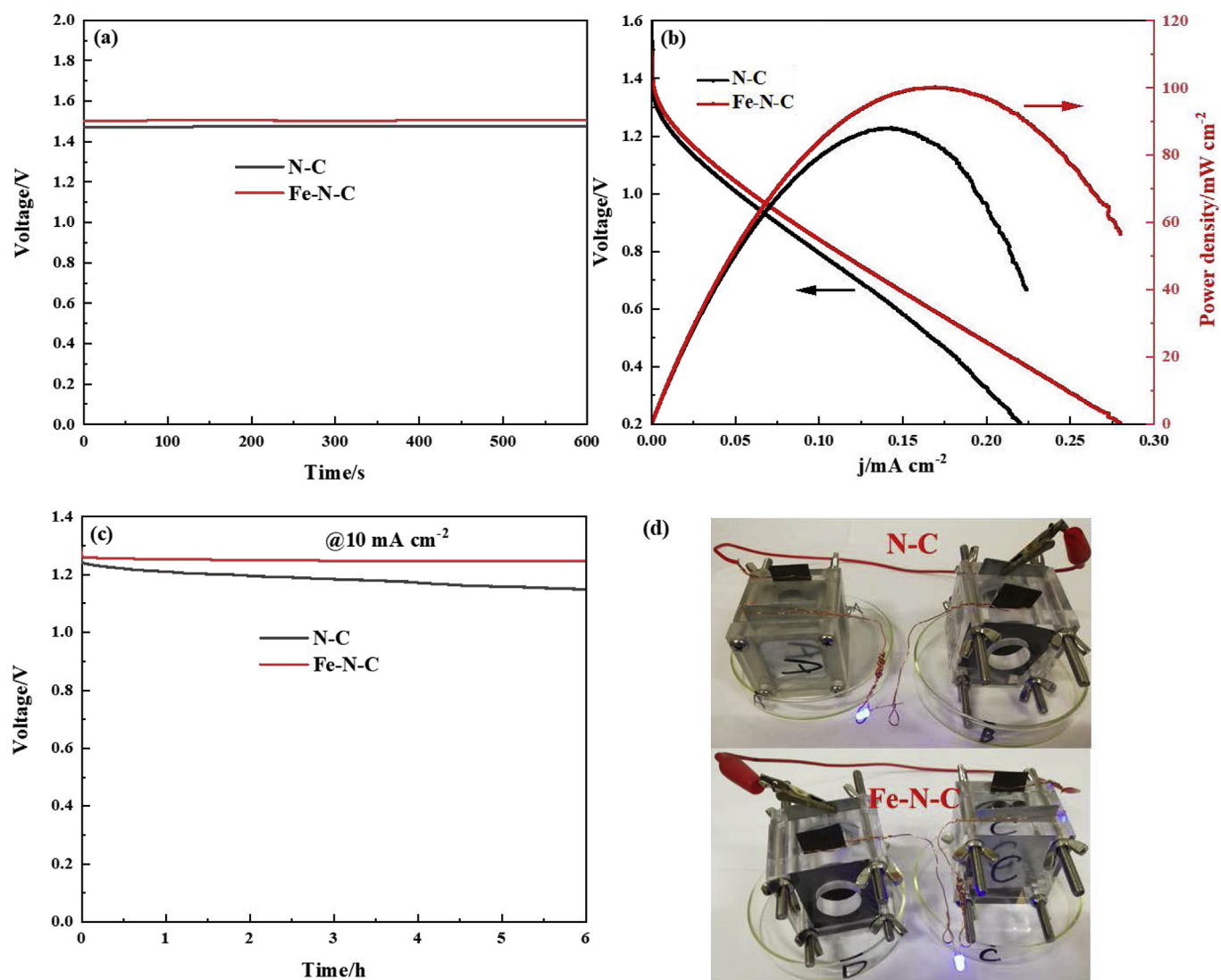


Fig. 9. Open-circuit voltage measurements (a) and polarization and power density curves (b) of the primary Zn-air batteries with N-C or Fe-N-C as the cathode catalyst; galvanostatic discharge curves at the specific discharge current density of 10 mA cm^{-2} (c); photograph of blue-light LED powered by two primary Zn-air batteries connected in series with N-C or Fe-N-C as the cathode catalyst (d). (A colour version of this figure can be viewed online.)

samples can be attributed to the highly dispersed Fe-/N-based species on the porous N-C nanosheets with high specific surface area and large pore volume, which can provide fully accessible active sites for ORR and ensure rapid pathway for the mass transportation of ORR-involved species. Moreover, both N-C and Fe-N-C as air cathode for Zn-air batteries exhibit high power density and good durability. This research work will provide a new avenue for the synthesis of porous N-C materials for promising applications in Zn-air batteries.

Acknowledgements

This work was supported by the National Natural Science Foundation of China (Grant number 21306144) and the Natural Science Foundation of Hubei Province (Grant number 2016CFB461).

Appendix A. Supplementary data

Supplementary data to this article can be found online at <https://doi.org/10.1016/j.carbon.2019.05.044>.

References

- [1] C. Hu, Y. Xiao, Y. Zou, L. Dai, Carbon-based metal-free electrocatalysis for energy conversion, energy storage, and environmental protection, *Electrochem. Energy Rev.* 1 (1) (2018) 84–112.
- [2] Y.-J. Wang, H. Fan, A. Ignaszak, L. Zhang, S. Shao, D.P. Wilkinson, et al., Compositing doped-carbon with metals, non-metals, metal oxides, metal nitrides and other materials to form bifunctional electrocatalysts to enhance metal-air battery oxygen reduction and evolution reactions, *Chem. Eng. J.* 348 (2018) 416–437.
- [3] J.-S. Lee, S. Tai Kim, R. Cao, N.-S. Choi, M. Liu, K.T. Lee, et al., Metal-air batteries with high energy density: Li-air versus Zn-air, *Adv. Energy Mater.* 1 (1) (2011) 34–50.
- [4] A.A. Gewirth, J.A. Varnell, A.M. DiAscro, Nonprecious metal catalysts for oxygen reduction in heterogeneous aqueous systems, *Chem. Rev.* 118 (5) (2018) 2313–2339.
- [5] L. Yang, D. Cheng, H. Xu, X. Zeng, X. Wan, J. Shui, et al., Unveiling the high-activity origin of single-atom iron catalysts for oxygen reduction reaction, *Proc. Natl. Acad. Sci. U.S.A.* 115 (26) (2018) 6626–6631.
- [6] G. Wu, K.L. More, C.M. Johnston, P. Zelenay, High-performance electrocatalysts for oxygen reduction derived from polyaniline, iron, and cobalt, *Science* 332 (6028) (2011) 443–447.
- [7] H.T. Chung, D.A. Cullen, D. Higgins, B.T. Sneed, E.F. Holby, K.L. More, et al., Direct atomic-level insight into the active sites of a high-performance PGM-free ORR catalyst, *Science* 357 (6350) (2017) 479–484.

- [8] D. Guo, R. Shibuya, C. Akiba, S. Saji, T. Kondo, J. Nakamura, Active sites of nitrogen-doped carbon materials for oxygen reduction reaction clarified using model catalysts, *Science* 351 (6271) (2016) 361–365.
- [9] Y. Zheng, Y. Jiao, Y. Zhu, Q. Cai, A. Vasileff, L.H. Li, et al., Molecule-level g-C₃N₄ coordinated transition metals as a new class of electrocatalysts for oxygen electrode reactions, *J. Am. Chem. Soc.* 139 (9) (2017) 3336–3339.
- [10] Y. Zheng, Y. Jiao, J. Chen, J. Liu, J. Liang, A. Du, et al., Nanoporous graphitic-C₃N₄@carbon metal-free electrocatalysts for highly efficient oxygen reduction, *J. Am. Chem. Soc.* 133 (50) (2011) 20116–20119.
- [11] J. Zhang, M. Zhang, G. Zhang, X. Wang, Synthesis of carbon nitride semiconductors in sulfur flux for water photoredox catalysis, *ACS Catal.* 2 (6) (2012) 940–948.
- [12] X. Yan, X. Xu, Q. Liu, J. Guo, L. Kang, J. Yao, Functionalization of multi-walled carbon nanotubes with iron phthalocyanine via a liquid chemical reaction for oxygen reduction in alkaline media, *J. Power Sources* 389 (2018) 260–266.
- [13] W. Wang, W. Chen, P. Miao, J. Luo, Z. Wei, S. Chen, NaCl crystallites as dual-functional and water-removable templates to synthesize a three-dimensional graphene-like macroporous Fe-N-C catalyst, *ACS Catal.* 7 (9) (2017) 6144–6149.
- [14] X. Sun, Y. Li, Colloidal carbon spheres and their core/shell structures with noble-metal nanoparticles, *Angew. Chem. Int. Ed.* 43 (5) (2004) 597–601.
- [15] W.J. Ong, L.L. Tan, Y.H. Ng, S.T. Yong, S.P. Chai, Graphitic carbon nitride (g-C₃N₄)-based photocatalysts for artificial photosynthesis and environmental remediation: are we a step closer to achieving sustainability? *Chem. Rev.* 116 (12) (2016) 7159–7329.
- [16] K.S. Sing, R.T. Williams, Physisorption hysteresis loops and the characterization of nanoporous materials, *Adsorpt. Sci. Technol.* 22 (10) (2004) 773–782.
- [17] K. Yuan, S. Sfaelou, M. Qiu, D. Lützenkirchen-Hecht, X. Zhuang, Y. Chen, et al., Synergetic contribution of boron and Fe-N_x species in porous carbons toward efficient electrocatalysts for oxygen reduction reaction, *ACS Energy Lett* 3 (1) (2018) 252–260.
- [18] H.-x. Zhong, J. Wang, Y.-w. Zhang, W.-l. Xu, W. Xing, D. Xu, et al., ZIF-8 derived graphene-based nitrogen-doped porous carbon sheets as highly efficient and durable oxygen reduction electrocatalysts, *Angew. Chem. Int. Ed.* 53 (51) (2014) 14235–14239.
- [19] D. Zhao, J. Dai, N. Zhou, N. Wang, P. Xinwen, Y. Qu, et al., Prussian blue analogues-derived carbon composite with cobalt nanoparticles as an efficient bifunctional electrocatalyst for oxygen reduction and hydrogen evolution, *Carbon* 142 (2019) 196–205.
- [20] Y. Li, Z. Li, Y. Wu, H. Wu, H. Zhang, T. Wu, et al., Carbon particles co-doped with N, B and Fe from metal-organic supramolecular polymers for boosted oxygen reduction performance, *J. Power Sources* 412 (2019) 623–630.
- [21] Y.-H. Qin, H.-H. Yang, X.-S. Zhang, P. Li, X.-G. Zhou, L. Niu, et al., Electrophoretic deposition of network-like carbon nanofibers as a palladium catalyst support for ethanol oxidation in alkaline media, *Carbon* 48 (12) (2010) 3323–3329.
- [22] K. Gong, F. Du, Z. Xia, M. Durstock, L. Dai, Nitrogen-doped carbon nanotube arrays with high electrocatalytic activity for oxygen reduction, *Science* 323 (5915) (2009) 760–764.
- [23] Y. Tang, R. Liu, S. Liu, B. Zheng, Y. Lu, R. Fu, et al., Cobalt and nitrogen codoped ultrathin porous carbon nanosheets as bifunctional electrocatalysts for oxygen reduction and evolution, *Carbon* 141 (2019) 704–711.
- [24] A. Elmouhahidi, E. Bailón-García, A.F. Pérez-Cadenas, J. Castelo-Quibén, F. Carrasco-Marín, Carbon-vanadium composites as non-precious catalysts for electro-reduction of oxygen, *Carbon* 144 (2019) 289–300.
- [25] J. Liu, Y. Liu, P. Li, L. Wang, H. Zhang, H. Liu, et al., Fe-N-doped porous carbon from petroleum asphalt for highly efficient oxygen reduction reaction, *Carbon* 126 (2018) 1–8.
- [26] Z.-Y. Sui, X. Li, Z.-Y. Sun, H.-C. Tao, P.-Y. Zhang, L. Zhao, et al., Nitrogen-doped and nanostructured carbons with high surface area for enhanced oxygen reduction reaction, *Carbon* 126 (2018) 111–118.
- [27] Y. Liu, B. Huang, X. Zhang, X. Huang, Z. Xie, In-situ fabrication of nitrogen-doped carbon nanosheets containing highly dispersed single iron atoms for oxygen reduction reaction, *J. Power Sources* 412 (2019) 125–133.
- [28] L. Lin, Q. Zhu, A.-W. Xu, Noble-metal-free Fe-N/C catalyst for highly efficient oxygen reduction reaction under both alkaline and acidic conditions, *J. Am. Chem. Soc.* 136 (31) (2014) 11027–11033.
- [29] S. Zhao, L. Yan, H. Luo, W. Mustain, H. Xu, Recent progress and perspectives of bifunctional oxygen reduction/evolution catalyst development for regenerative anion exchange membrane fuel cells, *Nanomater. Energy* 47 (2018) 172–198.
- [30] L. Yang, X. Zeng, W. Wang, D. Cao, Recent progress in MOF-derived, heteroatom-doped porous carbons as highly efficient electrocatalysts for oxygen reduction reaction in fuel cells, *Adv. Funct. Mater.* 28 (7) (2018) 1704537.
- [31] Q. Xue, Y. Ding, Y. Xue, F. Li, P. Chen, Y. Chen, 3D nitrogen-doped graphene aerogels as efficient electrocatalyst for the oxygen reduction reaction, *Carbon* 139 (2018) 137–144.
- [32] L. Lai, J.R. Potts, D. Zhan, L. Wang, C.K. Poh, C. Tang, et al., Exploration of the active center structure of nitrogen-doped graphene-based catalysts for oxygen reduction reaction, *Energy Environ. Sci.* 5 (7) (2012) 7936–7942.
- [33] H. Deng, Q. Li, J. Liu, F. Wang, Active sites for oxygen reduction reaction on nitrogen-doped carbon nanotubes derived from polyaniline, *Carbon* 112 (2017) 219–229.
- [34] B. Huang, X. Hu, Y. Liu, W. Qi, Z. Xie, Biomolecule-derived N/S co-doped CNT-graphene hybrids exhibiting excellent electrochemical activities, *J. Power Sources* 413 (2019) 408–417.
- [35] J. Li, J. Chen, H. Wan, J. Xiao, Y. Tang, M. Liu, et al., Boosting oxygen reduction activity of Fe-N-C by partial copper substitution to iron in Al-air batteries, *Appl. Catal. B Environ.* 242 (2019) 209–217.
- [36] J.-D. Yi, R. Xu, Q. Wu, T. Zhang, K.-T. Zang, J. Luo, et al., Atomically dispersed iron-nitrogen active sites within porphyrinic triazine-based frameworks for oxygen reduction reaction in both alkaline and acidic media, *ACS Energy Lett* 3 (4) (2018) 883–889.
- [37] X. Li, W. Bi, L. Zhang, S. Tao, W. Chu, Q. Zhang, et al., Single-atom Pt as co-catalyst for enhanced photocatalytic H₂ evolution, *Adv. Mater.* 28 (12) (2016) 2427–2431.
- [38] G. Vilé, D. Albani, M. Nachtegaal, Z. Chen, D. Dontsova, M. Antonietti, et al., A stable single-site palladium catalyst for hydrogenations, *Angew. Chem. Int. Ed.* 54 (38) (2015) 11265–11269.
- [39] S. Liu, I.S. Amiinu, X. Liu, J. Zhang, M. Bao, T. Meng, et al., Carbon nanotubes intercalated Co/N-doped porous carbon nanosheets as efficient electrocatalyst for oxygen reduction reaction and zinc-air batteries, *Chem. Eng. J.* 342 (2018) 163–170.
- [40] J. Zhang, Z. Zhao, Z. Xia, L. Dai, A metal-free bifunctional electrocatalyst for oxygen reduction and oxygen evolution reactions, *Nat. Nanotechnol.* 10 (5) (2015) 444–452.
- [41] H.B. Yang, J. Miao, S.-F. Hung, J. Chen, H.B. Tao, X. Wang, et al., Identification of catalytic sites for oxygen reduction and oxygen evolution in N-doped graphene materials: development of highly efficient metal-free bifunctional electrocatalyst, *Sci. Adv.* 2 (4) (2016) 1501122.
- [42] K. Fu, Y. Wang, L. Mao, X. Yang, J. Jin, S. Yang, et al., Strongly coupled Co, N co-doped carbon nanotubes/graphene-like carbon nanosheets as efficient oxygen reduction electrocatalysts for primary zinc-air battery, *Chem. Eng. J.* 351 (2018) 94–102.